Materials Today Communications 47 (2025) 112790

Contents lists available at ScienceDirect

Materials Today Communications

journal homepage: www.elsevier.com/locate/mtcomm

Deformation and damage of an Al/PTFE composite under uniaxial compression: An *in situ* synchrotron X-ray tomography study

G.D. Lai [a,b,c], H. Niu [d], K. Li [e], L. Lu [a,f], Y. Cai [c,f], Y.L. Bian [c,f,*], H.W. Chai [b,**]

[a] School of Physical Science and Technology, Southwest Jiaotong University, Chengdu, Sichuan, PR China
[b] Dynamic Materials Data Science Center, School of Materials Science and Engineering, Southwest Jiaotong University, Chengdu, Sichuan, PR China
[c] The Peac Institute of Multiscale Sciences, Chengdu, Sichuan, PR China
[d] China Academy of Space Technology, Beijing, PR China
[e] Shanghai Synchrotron Radiation Facility, Shanghai Advanced Research Institute, Chinese Academy of Sciences, Shanghai, PR China
[f] Key Laboratory of Extreme Material Dynamics Technology, Sichuan, PR China

A R T I C L E I N F O

Keywords:
Al/PTFE composite
in situ micro CT
Deformation and damage behavior
Microstructure

A B S T R A C T

The deformation and damage mechanisms of aluminum/polytetrafluoroethylene (Al/PTFE) composites under quasi-static compression are critical for aerospace, defense and structural applications, yet their mesoscale behavior remains insufficiently understood. This study combines *in situ* synchrotron X-ray micro computed tomography (CT) with CT-based finite element method (FEM) simulations to dynamically resolve the interplay between microstructure evolution and mechanical response. Real-time 3D imaging reveals negligible contributions of initial voids to bulk deformation, while catastrophic failure is governed by shear-induced interfacial debonding between Al particles and progressive void coalescence. Mesoscale FEM simulations quantify stress localization on Al particles, demonstrating its dependence on particle alignment relative to the loading direction. Damage initiates exclusively when adjacent particles deviate from the loading direction, underscoring the pivotal role of microstructural heterogeneity. These findings provide new insights into mesoscale structure–property relations in Al/PTFE composites, and the combined methodology of *in situ* CT experiments and CT image-based FEM simulations offers potential for advancing mechanistic studies of multiphase composites under complex mechanical conditions.

1. Introduction

Particle composites have received increasing attention over the past few decades in the aerospace [1], automotive manufacturing [2], energy industries [3], biomedical science [4] and other application fields [5–7], owing to their exceptional mechanical properties and diverse engineering applications. By incorporating particle reinforcement into the matrix, these composites demonstrate not only enhanced strength, hardness, and wear resistance [8], but also improved thermal and electrical conductivities [9–11]. The mechanical behavior of such composites is strongly influenced by the morphological characteristics, distribution and interfacial interactions of the embedded particles [12–15]. Consequently, studying the microscopic deformation and damage mechanisms of particle composites under different loading conditions is crucial to understanding and improving their macroscopic mechanical properties.

Aluminum and its alloys have become indispensable in engineering applications due to their high strength-to-weight ratio [16], outstanding corrosion resistance [17], and remarkable formability [18]. Recent innovations in aerospace structure [19], lightweight transportation systems [20], and additive manufacturing techniques [21] have further solidified their pivotal role as matrix/filler materials in multifunctional particle composites.

Aluminum/polytetrafluoroethylene (Al/PTFE) composites represent an important class of reactive materials, and have unique mechanical properties and functional characteristics [22–24]. In particular, these composites exhibit outstanding energy dissipation, dynamic responsiveness, and impact resistance under high strain rate loading (e.g. shock and blast loading), and are considered as promising candidates for applications in propellants, explosives and structural reinforcement [25–27].

Previous studies on the mechanical behavior of Al/PTFE composites primarily employed split Hopkinson pressure bar (SHPB) [28–

* Corresponding author at: The Peac Institute of Multiscale Sciences, Chengdu, Sichuan, PR China.
** Corresponding author.
E-mail addresses: ylbian@pims.ac.cn (Y.L. Bian), hwchai@swjtu.edu.cn (H.W. Chai).

https://doi.org/10.1016/j.mtcomm.2025.112790
Received 11 February 2025; Received in revised form 24 April 2025; Accepted 8 May 2025
Available online 2 June 2025

Nomenclature

3D	Three-dimensional
CT	Computed tomograph
FEM	Finite element method
JC	Johnson–Cook
LuAG:Ce	Cerium doped lutetium aluminum crystal
MTS	Material testing system
PEEK	Polyetheretherketon
PTFE	Polytetrafluoroethylene
ROI	Region of interest
SDEG	Stiffness degradation
SR	Synthronton radiation
A	Initial yield strength
B	Hardening modulus
D, D_1, D_2, D_3	Damage constants
D_{eq}	Equivalent diameter
D_{eq}^{N}	Normalized Equivalent diameter
E	Young's modulus
$G_{\alpha\beta}^{(i)}$	Gyration tensor
I_E	Elongation index
I_F	Flatness index
R_k (R_1, R_2, R_3)	Characteristic axes
S	Sphericity
$V^{(i)}$	Volume
c	Subscript, barycenter
f (f_{Al}, f_{void})	Local volume farction
h_{R_1}, h_{R_3}	Probability density distribution
i	Superscript, particle index
j	Subscript, voxel index
k, k'	Subscript, eigenvalues index
n	Hardening exponent
x, y, z	Coordinate axes
α, β	Subscript, corresponding to x-, y-, z-axis
λ_α, λ_β	Coordinate, corresponding to x-, y-, z-axis
v	Possion's radiation
ϕ, θ	Azimuthal angle and polar angle
ρ	Density
σ	Engineering stress
σ_f	Plastic flow stress
σ_M	Von Mises stress
σ^*	Stress triaxiality
ε	Engineering strain
ε_{eq}	Equivalent plastic strain
ε_{frac}	Fracture strain

31] and drop-weight testing [32–34]. Under such low-speed impact loading, Al/PTFE composites absorb energy and ignite through such mechanisms as shear excitation [35,36], pressure triggering [37] and chemical reaction induction [38]. The deformation and damage mechanisms under quasi-static compressive loading are also of relevance to certain storage/transport/service conditions, but investigations along this line are fairly limited.

Feng and coworkers [22,39–42] conducted a series of quasi-static compression experiments on Al/PTFE composites, revealing that their strength, toughness and reactivity, are influenced by sintering temperature, equivalent ratio, and Al particle size. Notably, a critical particle size of <14 μm was identified for quasi-static initiation. Additionally, Ge et al. [43] and Smolyanskii et al. [44] characterized Al/PTFE composites via scanning electron microscopy (SEM) and computer tomography (CT), respectively. They found that there were a large number of initial voids within the composites, which greatly affected the mechanical properties. These studies have advanced our understanding through quasi-static loading and *ex-situ* characterizations. However, there is still a high demand for understanding microstructure–property relations and underlying mechanisms at the mesoscale through *in situ* experiments and mesoscale simulations. In particular, how the distribution of particles inside the material, the interfacial interaction between particles and matrix, and the formation and evolution of cracks affect the mechanical behavior of the material has not been systematically investigated in depth.

Recently, synchrotron-based high-resolution CT has been increasingly used to characterize the three-dimensional (3D) structure of engineering materials including reactive material [45,46] (e.g. solid propellants [47,48], and plastic bonded explosives [49,50], etc.), offering a nondestructive means to analysis internal defects without compromising structural integrity or safety. For instance, Wang et al. [51] employed synchrotron monochromatic X-ray CT to resolve irradiation-induced microstructural changes in 3,3-bis(azidomethyl) oxetane and tetrahydrofuran copolyether propellants at single-particle resolution. Wang et al. [52] quantified the spatiotemporal fracture patterns of recycled aggregate concrete under uniaxial compression through *in situ* CT. Similarly, Liu et al. [53] characterized the compression process of two types of graded asphalt mixtures and established the relationship between the evolution of mixture damage and strength degradation. These studies collectively highlight synchrotron radiation CT's capability to resolve multiscale deformation mechanisms in heterogeneous materials under verses conditions.

Furthermore, finite element method (FEM) simulations based on CT images provide significant insights into experimental data [54,55]. Given the heterogeneous microstructures of Al/PTFE composites, including Al particles and initial voids, it is necessary to employ techniques such as *in situ* CT and CT-based-FEM to capture the 3D structural evolution of these materials under loading. Quantitative characterization of particle morphology and mesoscale deformation, and the effect of the particle arrangement on deformation and damage remain scarce in both experimental and simulation contexts.

In the present work, the deformation and damage behavior of the Al/PTFE composite under uniaxial compression is investigated through an integrated methodology combining *in situ* micro-CT and CT image-based FEM simulations. Real-time 3D imaging reveals the dynamic structural evolution of Al particles and voids, with gyration tensor analysis quantifying morphological changes and density field variations during compression. Experiment results identify compressive shear-induced interfacial debonding between Al particles as the dominant damage mechanism, while progressive void coalescence drives catastrophic failure. And the CT based mesoscale FEM simulations elucidate the stress concentration and their dependence on particle alignment heterogeneity. Damage initiates exclusively when adjacent particles deviate from alignment with the loading direction. These findings provide insights into mesoscale structure–property relations in such particle composites and offer potential for advancing mechanistic studies of multiphase composites under complex mechanical conditions.

2. Material and methodology

2.1. Material and initial characterization

The Al/PTFE composite is provided by the China Academy of Space Technology, and consists of the PTFE matrix and Al particles. Firstly, 70 vol% PTFE powder (particle size ≤ 5 μm, Shanghai Aladdin Biochemical Technology Co., Ltd.) and 30 vol% Al powder (Purity ≥ 99.75%, Foshan Chengfeng Material Technology Co., LTD) are mixed uniformly in anhydrous ethanol, followed by vacuum drying. The dried mixture is then cold-pressed into a circular mold using a hydraulic press and sintered in a vacuum tube furnace under an argon atmosphere. The sintering protocol involves heating to 360 °C at a constant rate of 50 °C h^{-1}, holding for 4 h, and cooling back to room temperature at the same rate, resulting in a circular composite disk with Φ100 mm × 60 mm (Φ

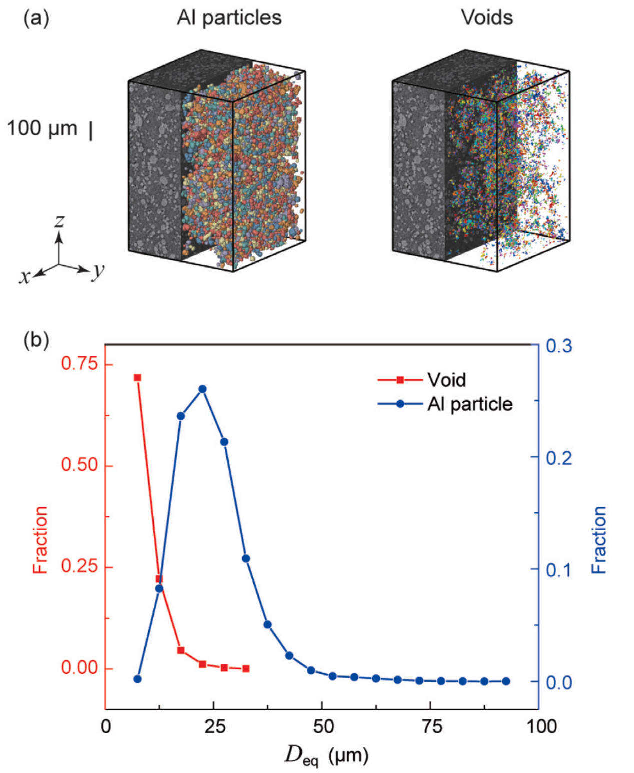

Fig. 1. CT characterization of the as-received Al/PTFE composite. (a) 3D renderings of Al particles and voids. (b) Equivalent diameter (D_{eq}) distribution of Al particles (blue) and voids (red). (For interpretation of the references to colour in this figure legend, the reader is referred to the web version of this article.)

denotes diameter). Finally, the disk is cut using a diamond wire saw into a cylinder with $\Phi 2\ \mathrm{mm} \times 2\ \mathrm{mm}$ for testing.

The initial CT characterization of the Al/PTFE composite is presented in Fig. 1a, including separate volume renderings of the AP particles, initial voids and their corresponding size distributions. The Al particles are dispersed within the PTFE matrix with 27.22 vol%. Meanwhile, numerous initial voids are detected throughout the material, and their spatial distribution performs a certain correlation with the Al particles. Moreover, no obvious cracks or interlayer defects are detected within the specimen, indicating that no additional defects were introduced during the fabrication process, thereby ensuring the representativeness of the experiment.

According to Fig. 1b, the equivalent diameters (D_{eq}, as defined in Section 2.3) of Al particles are distributed in the range of 0–100 μm, with its maximum at 25 μm. The D_{eq} values of initial voids are majority distributed with 0–10 μm. Given the small size of Al particles, the formation of initial voids is likely caused by the agglomeration of particles commonly observed in particle composites [43,44,56].

2.2. In situ CT testing

A home-made miniature material testing system (MTS) coupled with a high-precision imaging system is applied for *in situ* micro CT experiments at beamline BL16U2 of Shanghai Synchrotron Radiation Facility (Fig. 2). The specimen is compressed downward along the $-z$-axis at a strain rate of 0.001 s^{-1}. The force–displacement signals are output from the piezoelectric sensor and the stepper motor, and subsequently converted into an engineering stress–strain curve (Fig. 3). More experimental details were presented elsewhere [47,57].

The imaging system consists of a metal–oxide–semiconductor (CMOS) detector (Hamamatsu ORCA-Flash 4.0, 2048 × 2048 pixels, pixel size 6.5 μm) equipped with a 100 μm cerium doped lutetium

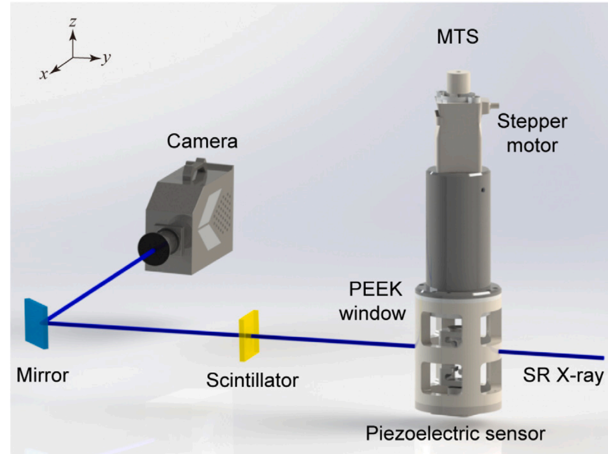

Fig. 2. Schematic setup for uniaxial compression loading with *in situ* synchrotron X-ray micro-CT. Loading is along the z-axis. PEEK: polyetheretherketone. SR: synchrotron radiation.

aluminum crystal (LuAG:Ce) scintillator and a 4× magnification lens set and a seven-axis electric displacement stage. The monochromatic X-ray energy is set at 15.24 KeV, and the field of view is ∼3.36 × 1.31 mm^2 (width × height) with a nominal pixel resolution of 1.64 μm. During a CT scan, the sample is rotated from 0 to 180°, and 1080 projections are captured. For a single projection, the exposure time is set as 100 ms. Two scans are performed along the sample height direction to cover the whole region at each deformation stage.

2.3. CT data analysis

Firstly, the projection is reconstructed via an open-source code, *TomoPy* [58], and the reconstructed images are subjected to a non-local mean filtering method [59] to improve the signal-to-noise ratio. The global thresholding and top-hat methods are then applied to extract Al particles, voids, and the PTFE matrix. The marker-controlled watershed and classical watershed methods are applied to refine the segmentation.

The gyration tensor analysis is conducted to quantify the 3D structure of each phase [60,61]. The gyration tensor can be written as

$$G_{\alpha\beta}^{(i)} = \frac{1}{V^{(i)}} \sum_{j=1}^{V^{(i)}} \left(\lambda_{\alpha_j}^{(i)} - \lambda_{\alpha_c}^{(i)} \right) \left(\lambda_{\beta_j}^{(i)} - \lambda_{\beta_c}^{(i)} \right). \tag{1}$$

Al particle i consists of $V^{(i)}$ voxels, and the coordinates of voxel j are denoted as $\lambda_{\alpha_j}^{(i)}$ or $\lambda_{\beta_j}^{(i)}$, where $\alpha,\ \beta = 1, 2, 3$ correspond to the x-, y- and z-axes, respectively. Similarly, $\lambda_{\alpha_c}^{(i)}$ or $\lambda_{\beta_c}^{(i)}$ is the barycenter of particle i. The eigenvectors of $G_{\alpha\beta}^{(i)}$ are obtained, and the corresponding eigenvalues are calculated as R_k (k = 1, 2, 3). Using these eigenvectors and eigenvalues, the characteristic ellipsoid of particle i is constructed [62], and the lengths of the semiaxes are $\sqrt{5R_k}$. Moreover, the orientation of semiaxis k is characterized with its polar angle θ_k and azimuthal angle ϕ_k. θ_k is the angle between the z-axis and the k-semiaxis, and ϕ_k is the angle between the orthogonal projection of the k-semiaxis onto the reference xy-plane and the x-axis.

The equivalent diameter (D_{eq}), sphericity (S), elongation index (I_E) and flatness index (I_F) are utilized to characterize the 3D structure of an object, defined as follows:

$$D_{eq} = (6V/\pi)^{-3}, \tag{2}$$

$$S = 1 - \frac{1}{2} \sum_{k>k'}^{3} (R_k - R_{k'})^2 \left(\sum_{k=1}^{3} R_k \right)^{-2}, \tag{3}$$

$$I_E = R_2/R_1, \tag{4}$$

$$I_F = R_3/R_2. \tag{5}$$

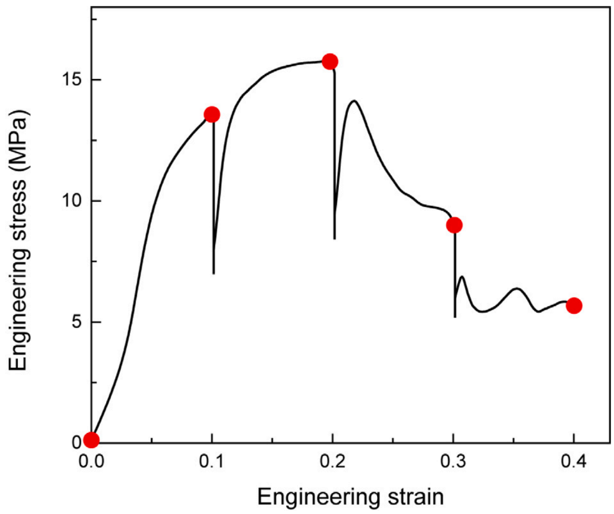

Fig. 3. Engineering stress–strain curve of the Al-PTFE composite under uniaxial compression. The red filled circles indicate the moments for *in situ* CT scans, corresponding to strains of 0%, 9.71%. 19.68%, 30.10% and 40.00%, respectively. (For interpretation of the references to colour in this figure legend, the reader is referred to the web version of this article.)

A detailed description of the structural indices can be found in relevant Refs. [47,63,64].

3. Result and discussion

3.1. Uniaxial compression loading with in situ CT

The engineering stress–strain (σ–ε) curve of the Al/PTFE composite under uniaxial compression is presented in Fig. 3, where the five CT scans are indicated by the red solid circles. The ultimate compressive strength is 15.78 MPa at a failure strain of 30.10%. The vertical drops in stress at each scan point correspond to stress relaxation during the pause intervals of the compression loading for the CT scanning, as commonly observed in such *in situ* CT experiments [64,65].

The 3D configurations of the Al/PTFE composite at different strains are shown in Fig. 4a, where the white spots correspond to Al particles, and the dark gray regions denote the PTFE matrix. At ε = 0%, Al particles are non-uniformly distributed within the matrix. The composite deforms elastically during the initial compression stage. As strain increases to ε = 30.10%, visible cracks emerge on the middle-left side and lower-right corner of the composite. Subsequently, catastrophic failure occurs.

Voids/cracks are extracted and plotted in Fig. 4b with color-coding based on the normalized equivalent void diameter $D_{\mathrm{eq}}^{\mathrm{N}}$ at each strain. At ε = 0%, initial voids are densely distributed throughout the composite. As strain increases to 19.68%, both the volume and number of voids increase considerably within the composite. At this stage, the composite reaches its ultimate strength. At ε = 30.10%, several distinct clusters of voids appear at the corners. With further damage accumulation, the voids coalesce and eventually propagate through the composite along the diagonal direction. Finally, the specimen undergoes complete fracture at ε = 40.00%.

Fig. 4c illustrates the evolution of Al particles within the composite during compression. As the specimen is compressed, all Al particles move primarily along the loading direction. Furthermore, some particles exhibit lateral displacement perpendicular to the loading direction, reflecting the redistribution and interaction of particles under compression.

Given the high density and heterogeneous distribution of both particles and voids, it is challenging to quantitatively evaluate the structural evolution of the Al/PTFE composite. To address this, localized volume fractions (f_{Al} or f_{void}) are employed to characterize the evolution of Al particles and voids. The configurations are partitioned into equally sized cubic bins with dimensions of 52 × 52 × 52 μm^3. For each bin, the respective volume fractions of particles and voids are calculated. The natural neighbor interpolation method [66] is then applied to reconstruct continuous 3D distributions of the volume fractions of particles and voids.

As shown in Fig. 5a, Al particle-dense regions (D1–D3) and particle-sparse regions (S1 and S2) are interlaced within the composite at ε = 0%. At ε = 9.71%, regions D1–D3 experience shear-like displacement under compression. The local particle density increases both at the edges of D1 and D3, and progressively towards their central zones. These dense regions are spatially segregated by S1 and S2. Upon further compression to ε = 19.68%, additional densification occurs. Al particles in regions D1 and D3 coalesce into discrete clusters, while the interstitial regions and D2 exhibit fragmentation. Ultimately, the Al particles reorganize into several particle aggregation domains (with Al high volume fraction).

Fig. 5b illustrates the spatiotemporal evolution of void volume fraction distributions at different strains. Prior to compression, initial voids exhibit a non-uniform spatial distribution across the composite, with slightly elevated void concentration in regions D2 and D3 relative to D1. During the initial compression stage (ε = 9.71%), the local void volume fraction diminishes, indicating porosity reduction via void closure. As compression progresses, a marked increase in void volume fraction is observed, predominantly within region S1 and select subdomains of D1 and D3. Ultimately, void coalescence drives crack nucleation, resultant void volume fraction distribution strongly correlates with the spatial arrangement of Al particles.

3.2. Evolution of al particles and voids

To better reveal the microstructure evolution in the Al/PTFE composite during compression, three sets of particles and their associated voids are tracked within regions D1, D2 and S1. Fig. 6a corresponds to a particle set adjacent to S1 in D1, Fig. 6b refers to the particle set in S1, and Fig. 6c depicts a particle set located in the middle of D2. At initial strain (0%), sparsely distributed small voids are identified adjacent to particles within the S1 region, whereas D1 and D2 exhibited densely populated voids with comparatively larger dimensions. Additionally, these voids are located preferentially on the surfaces of Al particles, with void density positively correlated to particle packing density. This spatial correlation suggests that particle aggregation promotes initial void nucleation.

According to Fig. 6a, the preexisting voids exhibit random surface distribution on Al particles. Voids located at the top of particle P1 undergo preferential compression due to axis-aligned loading, as marked by the pink dashed circle at ε = 9.71%. Simultaneously, an elongated void is generated on the surface of particle P2, indicated by the yellow dashed ellipse. At ε = 19.68%, several toroidal void clusters develop near the hemispherical surface of particles P3 and P4 (the black arrows). At this point, the composite reaches its ultimate compressive strength. The particle set experiences a displacement along the normal plane in the loading direction with a slight rotation, as a result of stress release facilitated by interfacial debonding. Eventually, some newly-developed voids coalesce with the initial voids, forming larger defects and initiating structural damage.

At the early stage of compression, the preexisting voids largely remain unchanged (Fig. 6b, ε = 0% – 9.71%). Progressive deformation induces particle P5-P7 convergence, triggering interfacial debonding at P5. At ε = 30.10%, particle P8 overrides P5, while P6 ejects from the view via shear-induced displacement.

Deformation at the early stage (ε = 0% – 9.71%, Fig. 6c) is primarily governed by particle displacement and rotation. After the composite reaches the ultimate compressive strength, mutual extrusion between particles P10 and P11 occurs, concurrently inducing interfacial

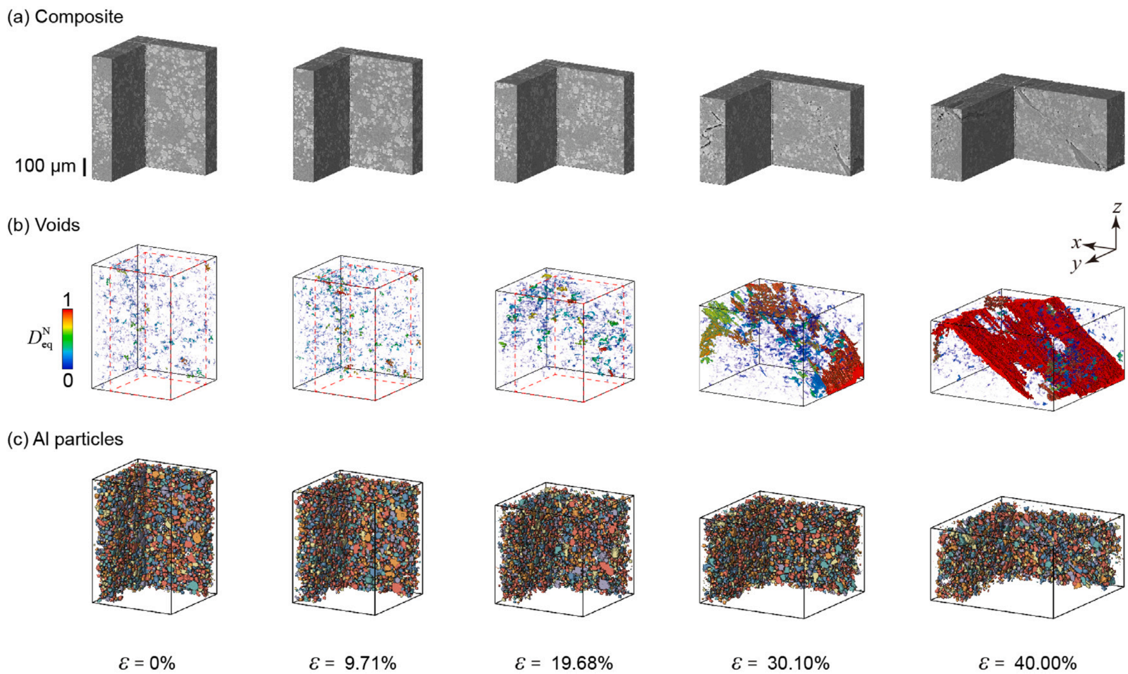

Fig. 4. 3D configurations of the Al-PTFE composite at different strains. (a) The composite. (b) Voids. Color coding refers to the normalized equivalent diameter (D_{eq}^{N}). (c) Al particles. Color coding refers to different particles. (For interpretation of the references to colour in this figure legend, the reader is referred to the web version of this article.)

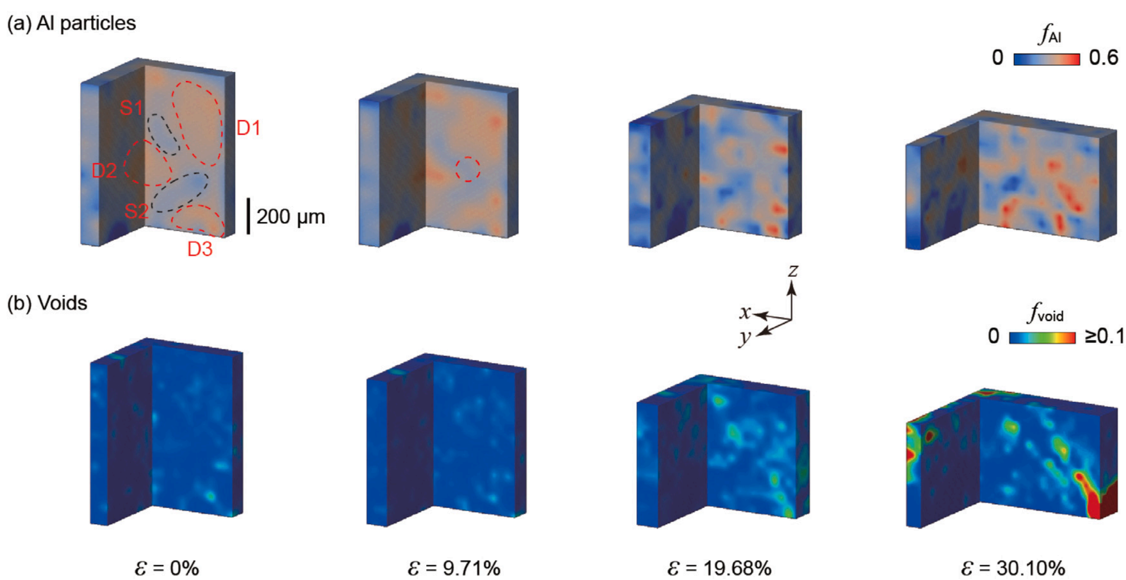

Fig. 5. Spatial distributions of local volume fractions of Al particles and voids at different strains. (a) Al particles (f_{Al}). D1, D2, and D3 show diverse dense particle compaction regions at $\varepsilon = 0\%$, while S1 and S2 show different loose particle compaction regions at $\varepsilon = 0\%$. (b) Voids (f_{void}).

debonding at P9. Subsequently, P10 interacts with P11 and effectively displaces its original position. Concurrently, particle P9 exhibits progressive interfacial failure, with voids expanding and coalescing despite positional invariance.

The above analysis reveals that stress release in the Al/PTFE composite subjected to compression is predominantly governed by interfacial debonding and inhomogeneous displacement and rotation of Al particles. Inhomogeneous particle displacement induces deformation and interparticle extrusion, while interfacial debonding catalyzes crack formation and ultimately drives catastrophic structural failure of the composite.

Fig. 7 statistically characterizes four morphological parameters of Al particles at different strains: equivalent diameter (D_{eq}), sphericity (S), elongation index (I_E), and flattening index (I_F). During the elastic regime ($\varepsilon < 9.71\%$), Al particle morphology remains essentially invariant Deformation occurs only after the composite reaches its ultimate compressive strength. After 19.66% strain, the fraction of small Al particles ($D_{eq} < 15$ μm) increases significantly, with concurrent decreases in S, I_E and I_F. These compaction-induced flattening correlate with localized Al volume fraction increases in specific regions after 19.66% strain, as shown in Fig. 5a.

The structural evolution of voids within the Al/PTFE composite is presented in Fig. 8a–d. During the initial stage of compression (ε = 0%–9.71%), annihilation of the preexisting voids and formation of new voids are observed, and the overall distribution of D_{eq} of the voids remains largely unchanged. Subsequent loading (ε = 19.66%–30.10%)

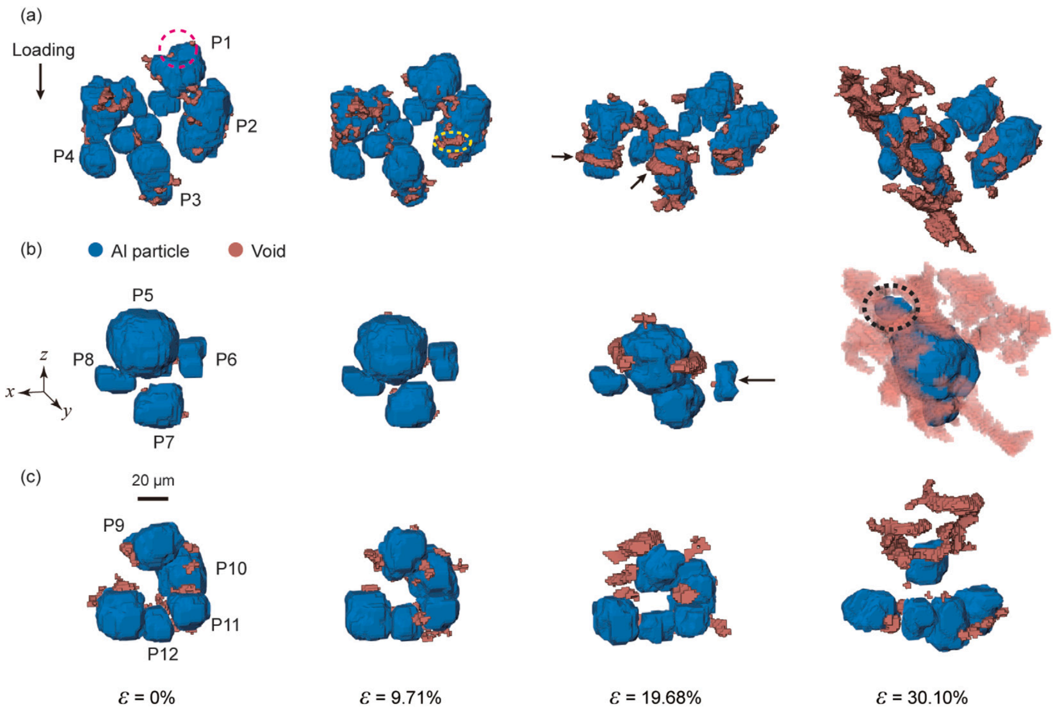

Fig. 6. Void evolution in the regions as defined in Fig. 5a. (a) Region D1. (b) Region S1. (c) Region D2. Blue indicates Al particles, while red represents voids. Labels P1–P12 correspond to twelve selected Al particles tracked during the deformation process. (For interpretation of the references to colour in this figure legend, the reader is referred to the web version of this article.)

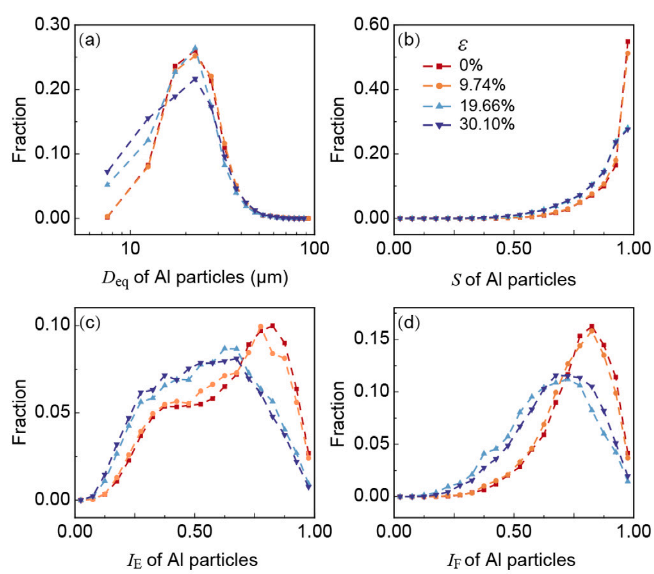

Fig. 7. Statistical analysis of Al particle morphology at different strains. (a) Equivalent diameter (D_{eq}). (b) Sphericity (S). (c) Elongation index (I_E). (d) Flatness index (I_F).

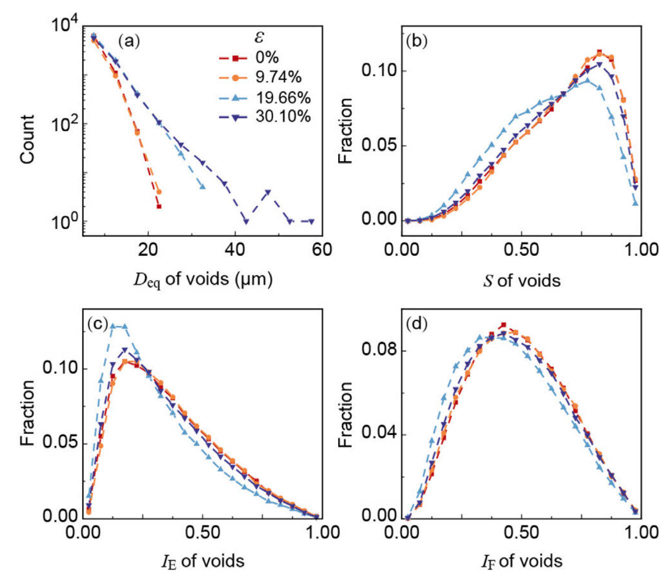

Fig. 8. Statistical analysis of void morphology at different strains. (a) Equivalent diameter (D_{eq}). (b) Sphericity (S). (c) Elongation index (I_E). (d) Flatness index (I_F).

drives stress-mediated void coalescence, yielding both increased mean void size and population density. As seen from the distributions of S, I_E and I_F, voids gradually deform from nearly spherical to ellipsoidal shapes as strain increases from 0 to 19.66%. After 19.66% strain, rightward shifting of I_E and I_F peaks indicates coalescence-triggered void annihilation, with residual voids undergoing collapse through stress redistribution.

Considering the rotation of Al particles and the deformation of voids, the orientations of the R_1-axes (the long semi-axes) of Al particles at different strains are analyzed (Fig. 9a). Initially, the R_1-axes of Al particles show preferential orientation with yz-plane parallel to the load direction, with several high-probability-density regions near $\theta_1 = 45°$ and 90°. During the early compression stage ($\varepsilon = 9.71\%$), constrained particle rotation prevails due to PTFE matrix interlocking. By $\varepsilon = 19.68\%$, as the composite reaches the ultimate compressive strength, neighboring particle interactions drive axis reorientation. This rotational homogenization eliminates initial angular preferences of the R_1-axes of Al particles, as evidenced by probability density flattening. With further compression, the R_1-axis orientations become more uniform.

Given the annihilation of initial voids and the formation of new voids during compression, the R_3-axes (the shortest semi-axes) of voids

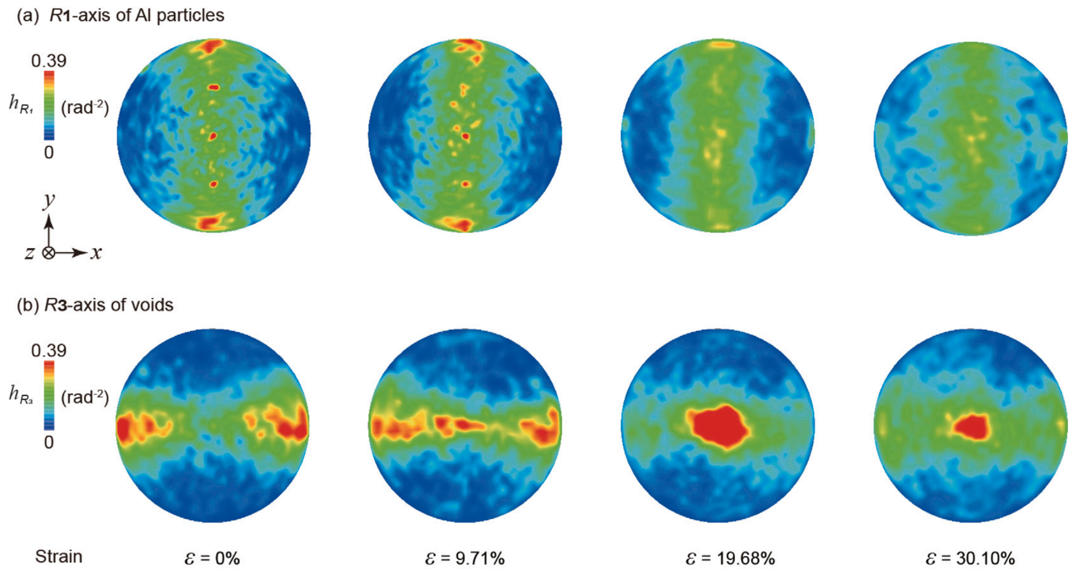

Fig. 9. Pole figures of the orientations of (a) the R_1-axes of Al particles, and (b) the R_3-axes of voids at different strains. Color-coding refers to probability density. (For interpretation of the references to colour in this figure legend, the reader is referred to the web version of this article.)

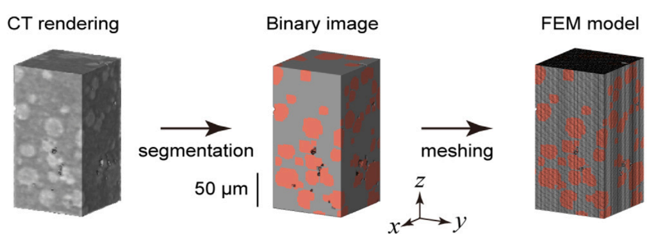

Fig. 10. Scheme for converting a CT image into an FEM model. Pink: Al particles; gray: PTFE matrix. (For interpretation of the references to colour in this figure legend, the reader is referred to the web version of this article.)

Table 1
Material parameters of the Al particles and the PTFE matrix for FEM analysis [43,70–75]. ρ: density; E: Young's modulus; ν: Poisson's ratio. See Eqs. (5) and (6) for other parameters.

Parameters	Al	PTFE
ρ (g cm^{-3})	2.7	2.2
E (GPa)	70	0.315
ν	0.34	0.41
A (MPa)	265	8
B (MPa)	426	30
n	0.34	1
D_1	...	0.45
D_2	...	0.25
D_3	...	4.65

are analyzed and shown in Fig. 9b. Initially, the R_3-axes predominantly align within the xz-plane perpendicular to the loading axis. As the strain exceeds 9.71%, the orientations of the R_3-axes gradually converge to the loading direction (the z-axis) driven by progressive deformation. This reflects void flattening anisotropy induced by axial compression, where void aspect ratios decrease preferentially along the loading direction regardless of initial orientations. Debonding-induced voids amplify this alignment tendency through stress-concentration effects. At 30.10% strain, the coalescence of some voids leads to a redistribution of the orientations of their R_3-axes, causing partial dispersion of the R_3-axes.

3.3. FEM analysis

To reveal more detailed deformation mechanisms of the Al/PTFE composite under quasi-static compression, the CT images are employed to construct a 3D finite element method (FEM) model. A region measuring 105 × 105 × 210 μm^3 is randomly extracted from the central region of the composite for analysis. The modeling procedure is shown in Fig. 10. First, a region of interest (ROI) image is cropped from the binarized CT image. Next, the binarized image is discretized into a 3D grid, where the vertices of each voxel serve as nodes, and each voxel is defined by 8 neighboring nodes, forming a hexahedral element. The FEM model comprises 130 Al particles with 528 384 elements.

Two rigid plates are added to the top and bottom surfaces of the ROI along the loading axis to simulate the compression experiment. The boundary conditions are set as free boundaries to capture the inhomogeneous deformation during compression. A strain of 30% is applied with a strain rate of 0.001 s^{-1}. The FEM analysis uses the explicit method with mass scaling enabled, using a scaling factor of 0.0001.

The Johnson–Cook (JC) constitutive model [67] and progressive damage model [68] are used to describe the deformation and damage of Al particles and the PTFE matrix. The flow stress (σ_f) in the simplified JC constitutive model, excluding the strain rate hardening and thermal softening items, is expressed as [69]

$$\sigma_f = A + B\varepsilon_{eq}^n. \tag{6}$$

where A is initial yield strength, and B and n are the hardening modulus and hardening exponent, respectively. ε_{eq} refers to the equivalent plastic strain.

Similarly, the fracture strain (ε_{frac}) is described as [70]

$$\varepsilon_{frac} = D_1 + D_2 \exp(D_3\sigma^*). \tag{7}$$

Here D_1–D_3 are damage parameters, and σ^* denotes stress triaxiality. Failure occurs when the damage parameter, $D = \int d\varepsilon_{eq}/\varepsilon_{frac}$, reaches unity. Given the significant difference in Young's modulus between Al and PTFE, only the damage of PTFE is considered in the FEM analysis. The corresponding material parameters are listed in Table 1 [43,70–75].

The simulation results, including the distribution of von Mises stress (σ_M), equivalent plastic strain (ε_{eq}), and stiffness degradation (SDEG), are illustrated in Fig. 11a–c for different strains.

According to Fig. 11a, stress concentrations are evident as early as at 5% strain. The stress is primarily concentrated on the Al particles

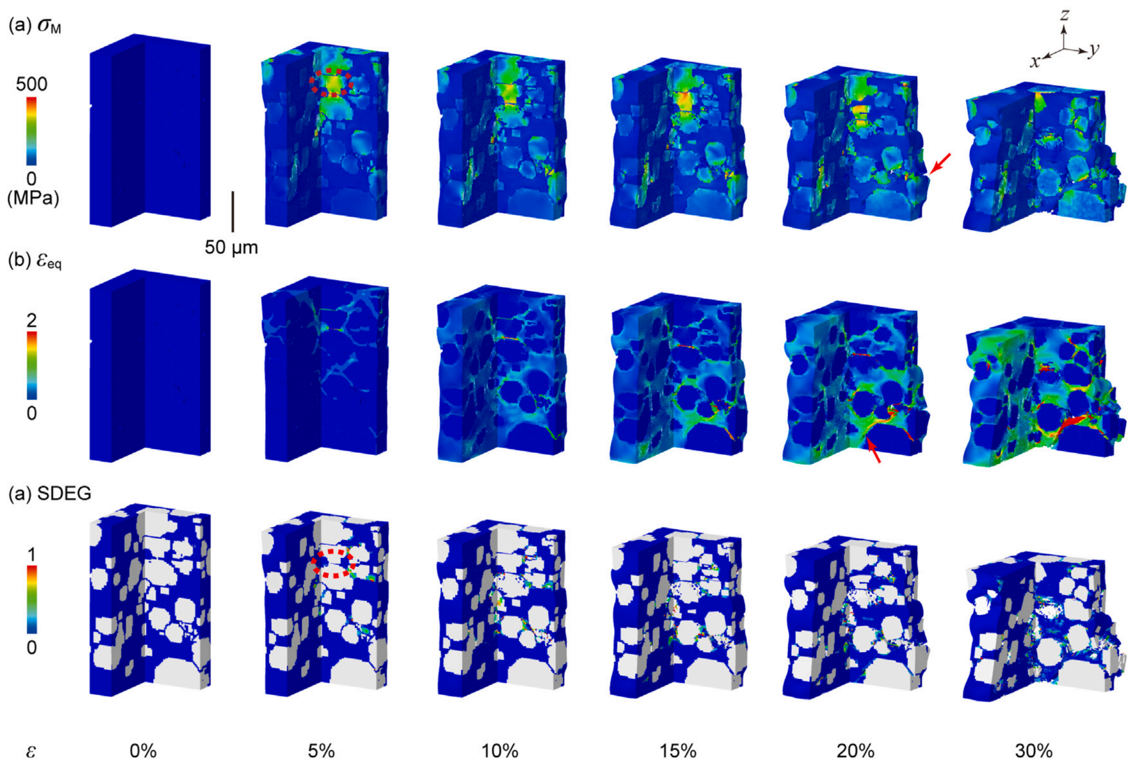

Fig. 11. Configurations of the Al/PTFE composite subjected to different strains obtained from FEM. Color coding is based on (a) von Mises stress (σ_M), (b) equivalent plastic strain (ε_{eq}), and (c) stiffness degradation (SDEG). (For interpretation of the references to colour in this figure legend, the reader is referred to the web version of this article.)

and gradually decreases from the particle surface towards the interior. As the deformation progresses, particles undergo mutual compression (e.g., marked by the red circle), experiencing significant stress ~500 MPa. At 20% strain, the marked particle within the ROI exhibits noticeable rotation, while an Al particle near the right edge (indicated by the red arrows) experiences interfacial debonding. The distribution of ε_{eq} in Fig. 11b shows the localization of plastic deformation in the PTFE matrix. At $\varepsilon = 20\%$, the wrinkling of the matrix material on the surface of an Al particle is observed (the red arrow), followed by interfacial debonding subsequently ($\varepsilon = 30\%$). However, no significant stress concentration is detected in this region, as a result of discontinuous displacement between the Al particle and the PTFE matrix interface.

Although the simulated stress concentrations should be interpreted with consideration of model simplifications, including the usage of a simplified JC constitutive model and idealized particle-matrix interfaces. These assumptions may affect quantitative accuracy but do not compromise the qualitative trends aligned with experimental observations.

The damage of the PTFE matrix described by SDEG is shown in Fig. 11c. During compression, the distribution of SDEG is localized within the PTFE matrix. Notably, no changes in SDEG are observed around the marked particles during the 5%–20% strain range, despite significant stress concentrations and plastic deformation in this region. At $\varepsilon = 20\%$, the SDEG begins to increase in response to the rotation of the marked particles. By comparing the microstructure of the marked particles with the remaining damaged regions, we observe that the alignment of neighboring particles near the damaged sites consistently form a finite angle with the loading direction. It suggests that the damage is primarily driven by the interfacial debonding induced by shearing between neighboring particles. Damage occurs only when the orientations of the adjacent particles deviate away from the loading direction.

4. Conclusions

The mechanical response of an Al/PTFE composite to uniaxial compression is investigated using *in situ* micro-CT, and the morphological and structural characteristics of Al particles and voids are obtained through a gyration tensor. The CT-image-based-FEM modeling to reveal the deformation and damage mechanisms. The main conclusions are summarized as follows:

- The deformation of the Al/PTFE composite under quasi-static compression is initially achieved via mutual compression between regions with high particle density, which transitions to compression within the regions at later stages. Compression induces the plastic deformation of Al particles and the collapse of initial voids.
- The damage manifests as interfacial debonding and crack coalescence. Interfacial debonding dominates damage evolution, driven by the mutual shear displacement between Al particles, particularly when the alignment of neighboring particles deviates from the loading direction.
- The integrated *in situ* CT based FEM simulations framework quantitatively links 3D microstructural evolution (via gyration tensor analysis) to mesoscale stress localization, revealing particle-dependent stress distribution and matrix damage initiation.

These results emphasize the critical role of particle alignment and void distribution in tailoring mechanical performance. Optimizing fabrication processes to minimize particle misorientation and initial voids could enhance compressive strength and damage tolerance.

CRediT authorship contribution statement

G.D. Lai: Writing – original draft, Visualization, Validation, Software, Methodology, Investigation, Data curation, Conceptualization. **H. Niu:** Resources. **K. Li:** Resources. **L. Lu:** Supervision, Conceptualization. **Y. Cai:** Investigation. **Y.L. Bian:** Investigation. **H.W. Chai:** Writing – review & editing, Conceptualization.

Declaration of competing interest

The authors declare that they have no known competing financial interests or personal relationships that could have appeared to influence the work reported in this paper.

Acknowledgments

This work was partially supported by Sichuan Science and Technology Program (Grant No. 2023YFG0077 and 2023NSFSC1284), and Guangxi Science and Technology Major Program (Grant No. AA23073019).

Data availability

Data will be made available on request.

References

[1] R. Yadav, M. Tirumali, X. Wang, M. Naebe, B. Kandasubramanian, Polymer composite for antistatic application in aerospace, Def. Technol. 16 (1) (2020) 107–118.
[2] H. Singh, G.S. Brar, H. Kumar, V. Aggarwal, A review on metal matrix composite for automobile applications, Mater. Today: Proc. 43 (2021) 320–325.
[3] S. Srivastava, J.L. Schaefer, Z. Yang, Z. Tu, L.A. Archer, 25Th anniversary article: polymer–particle composites: phase stability and applications in electrochemical energy storage, Adv. Mater. 26 (2) (2014) 201–234.
[4] J.B. Park, R.S. Lakes, Composites as biomaterials, Biomaterials (2007) 207–224.
[5] Y. Singh, J. Singh, S. Sharma, T.-D. Lam, D.-N. Nguyen, Fabrication and characterization of coir/carbon-fiber reinforced epoxy based hybrid composite for helmet shells and sports-good applications: Influence of fiber surface modifications on the mechanical, thermal and morphological properties, J. Mater. Res. Technol. 9 (6) (2020) 15593–15603.
[6] A. Saha, N.D. Kulkarni, P. Kumari, Development of bambusa tulda fiber-micro particle reinforced hybrid green composite: A sustainable solution for tomorrow's challenges in construction and building engineering, Constr. Build. Mater. 441 (2024) 137486.
[7] R. Kurahatti, A. Surendranathan, S. Kori, N. Singh, A. Kumar, S. Srivastava, Defence applications of polymer nanocomposites, Def. Sci. J. 60 (5) (2010) 551–563.
[8] Y. Thooyavan, L. Kumaraswamidhas, R.E. Raj, J. Binoj, Influence of SiC micro and nano particles on tribological, water absorption and mechanical properties of basalt bidirectional mat/vinyl ester composites, Compos. Sci. Technol. 219 (2022) 109210.
[9] X. Du, W. Yang, J. Zhu, L. Fu, D. Li, L. Zhou, Aligning diamond particles inside BN honeycomb for significantly improving thermal conductivity of epoxy composite, Compos. Sci. Technol. 222 (2022) 109370.
[10] Y. Wang, T. Liu, H. Zhang, N. Luo, F. Chen, Q. Fu, Effect of spherical alumina crystalline phase content and particle size distribution polydispersity on the properties of silicone rubber composites, Compos. Sci. Technol. 243 (2023) 110273.
[11] C. Garzón, H. Palza, Electrical behavior of polypropylene composites melt mixed with carbon-based particles: Effect of the kind of particle and annealing process, Compos. Sci. Technol. 99 (2014) 117–123.
[12] S.Y. Fu, X.Q. Feng, B. Lauke, Y.W. Mai, Effects of particle size, particle/matrix interface adhesion and particle loading on mechanical properties of particulate–polymer composites, Compos. Part B: Eng. 39 (6) (2008) 933–961.
[13] Y. Li, Effects of particle shape and size distribution on the shear strength behavior of composite soils, Bull. Eng. Geol. Environ. 72 (2013) 371–381.
[14] B. Pukanszky, G. VÖRÖS, Mechanism of interfacial interactions in particulate filled composites, Compos. Interfaces 1 (5) (1993) 411–427.
[15] J.N. Dastgerdi, G. Marquis, B. Anbarlooie, S. Sankaranarayanan, M. Gupta, Microstructure-sensitive investigation on the plastic deformation and damage initiation of amorphous particles reinforced composites, Compos. Struct. 142 (2016) 130–139.
[16] H. Sun, H. Li, H. Yang, J. Ma, X. Hao, M. Fu, Breaking through the bending limit of al-alloy tubes by cryogenic effect controlled mechanical properties and friction behaviours, Int. J. Mach. Tools Manuf. 195 (2024) 104111.
[17] X. Xu, W. Li, B. Wan, S. Jin, K. Chen, F. Su, Extremely improved the corrosion resistance and anti-wear behavior of aluminum alloy in 3.5% NaCl solution via amorphous craln coating protection, Corros. Sci. 230 (2024) 111952.
[18] Z. Hu, J. Zheng, L. Hua, Q. Sun, Investigation of forging formability, microstructures and mechanical properties of pre-hardening Al-Zn-Mg-Cu alloy, J. Manuf. Process. 131 (2024) 2082–2100.
[19] M. Mohammadi-pour, A. Khodabandeh, S. Mohammadi-pour, M. Paidar, Microstructure and mechanical properties of joints welded by friction-stir welding in aluminum alloy 7075-T6 plates for aerospace application, Rare Met. 44 (3) (2025) 2085–2093.
[20] Y. Yu, J. Li, Z. Xie, G. Gao, M.R. Sheikhi, J. Li, Ballistic performance of aluminum alloy plates with polyurea coatings for high-speed train structures, Compos. Struct. 351 (2025) 118553.
[21] W. Huang, M. Fang, H. Zhong, Y. Jia, S. Sun, Z. Jiang, Heat transfer and flow of molten pool in single track multi-layer aluminum alloy laser wire additive manufacturing, Opt. Laser Technol. 181 (2025) 111858.
[22] H.X. Wang, X. Fang, B. Feng, Z.R. Gao, S.Z. Wu, Y.C. Li, Influence of temperature on the mechanical properties and reactive behavior of Al-PTFE under quasi-static compression, Polymers 10 (1) (2018) 56.
[23] J. Wang, L. Zhang, Y. Mao, F. Gong, An effective way to enhance energy output and combustion characteristics of Al/PTFE, Combust. Flame 214 (2020) 419–425.
[24] W. Huang, Y.-f. Mao, J. Chen, J. Wang, W. Cao, X. q. Zhang, J. Wang, PTFE-modified Al through bridging approach to enhance combustion reaction and energetic performance, Chem. Eng. J. 497 (2024) 154459.
[25] J.X. Wu, Q. Liu, B. Feng, Q. Yin, Y.C. Li, S.Z. Wu, Z.S. Yu, J.Y. Huang, X.X. Ren, Improving the energy release characteristics of PTFE/Al by doping magnesium hydride, Def. Technol. 18 (2) (2022) 219–228.
[26] E. Dhanumalayan, G.M. Joshi, Performance properties and applications of polytetrafluoroethylene (PTFE)—a review, Adv. Compos. Hybrid Mater. 1 (2018) 247–268.
[27] T.R. Sippel, S.F. Son, L.J. Groven, Aluminum agglomeration reduction in a composite propellant using tailored Al/PTFE particles, Combust. Flame 161 (1) (2014) 311–321.
[28] E. Tang, Z. Sun, Y. Han, W. Yu, C. Chen, M. Xu, M. Chang, K. Guo, L. He, Dynamic characteristics of enhanced Al/PTFE and real-time quantitative evaluation of impact release energy under vacuum environment, Results Phys. 31 (2021) 105019.
[29] E. Tang, S. Li, C. Chen, Y. Han, Dynamic compressive behavior of fiber reinforced Al/PTFE active materials, J. Mater. Res. Technol. 9 (4) (2020) 8391–8400.
[30] J. Wu, H. Wang, B. Feng, Y. Li, S. Wu, Q. Yin, Z. Yu, J. Huang, The effect of temperature-induced phase transition of ptfe on the dynamic mechanical behavior and impact-induced initiation characteristics of Al/PTFE, Polym. Test. 91 (2020) 106835.
[31] X. Zhang, J. Zhang, L. Qiao, A. Shi, Y. Zhang, Y. He, Z. Guan, Experimental study of the compression properties of Al/W/PTFE granular composites under elevated strain rates, Mater. Sci. Eng.: A 581 (2013) 48–55.
[32] B. Feng, C.L. Qiu, T.H. Zhang, Y.F. Hu, H.G. Li, B.C. Xu, Sensitivity of Al-PTFE upon low-speed impact, Propellants, Explos. Pyrotech. 44 (5) (2019) 630–636.
[33] J.X. Wu, X. Fang, Z.R. Gao, H.X. Wang, J.Y. Huang, S.Z. Wu, Y.C. Li, Investigation on mechanical properties and reaction characteristics of Al-PTFE composites with different Al particle size, Adv. Mater. Sci. Eng. 2018 (1) (2018) 2767563.
[34] J. Cai, F. Jiang, K.S. Vecchio, M.A. Meyers, V.F. Nesterenko, Mechanical and microstructural properties of PTFE/Al/W system, in: AIP Conference Proceedings, Vol. 955, American Institute of Physics, 2007, pp. 723–726.
[35] H. Geng, R. Liu, Y. Ren, P. Chen, C. Ge, H. Wang, Dynamic compression-shear ignition mechanism of Al/PTFE reactive materials, Compos. Struct. 331 (2024) 117908.
[36] L. Tang, H. Wang, G. Lu, H. Zhang, C. Ge, Mesoscale study on the shock response and initiation behavior of Al-PTFE granular composites, Mater. Des. 200 (2021) 109446.
[37] G. Goviazin, R. Ceder, S. Kalabukhov, S. Hayun, D. Rittel, Challenging the paradigm for reactive material's ignition from shear to pressure: Thermomechanical study of Al-PTFE, J. Mech. Phys. Solids 186 (2024) 105581.
[38] G. Lu, P. Li, Z. Liu, J. Xie, C. Ge, H. Wang, Theoretical model for the impact-initiated chemical reaction of Al/PTFE reactive material, Materials 15 (15) (2022) 5356.
[39] B. Feng, Y.C. Li, S.Z. Wu, H.X. Wang, Z.M. Tao, X. Fang, A crack-induced initiation mechanism of Al-PTFE under quasi-static compression and the investigation of influencing factors, Mater. Des. 108 (2016) 411–417.
[40] B. Feng, X. Fang, Y. c. Li, S. z. Wu, Y. m. Mao, H. x. Wang, Reactions of Al-PTFE under impact and quasi-static compression, Adv. Mater. Sci. Eng. 2015 (1) (2015) 582320.
[41] B. Feng, Y.C. Li, H. Hao, H.X. Wang, Y.F. Hao, X. Fang, A mechanism of hot-spots formation at the crack tip of Al-PTFE under quasi-static compression, Propellants Explos. Pyrotech. 42 (12) (2017) 1366–1372.
[42] B. Feng, X. Fang, Y. c. Li, H. x. Wang, Y. m. Mao, S. z. Wu, An initiation phenomenon of Al-PTFE under quasi-static compression, Chem. Phys. Lett. 637 (2015) 38–41.
[43] C. Ge, Y. Dong, W. Maimaitituersun, Microscaaie simulation on mechanical properties of Al/PTFE composite based on real microstructures, Materials 9 (7) (2016) 590.
[44] A.S. Smolyanskii, E.D. Politova, O.A. Koshkina, M.A. Arsentyev, P.P. Kusch, L.V. Moskvitin, S.V. Slesarenko, D.P. Kiryukhin, L.I. Trakhtenberg, Structure of polytetrafluoroethylene modified by the combined action of γ-radiation and high temperatures, Polymers 13 (21) (2021) 3678.

[45] C. Confalonieri, E. Boller, Y. Cheng, E. Gariboldi, Synchrotron radiation micro-CT with phase contrast for high-temperature in-situ microstructural characterization of AlSn composite phase change materials, Mater. Charact. 193 (2022) 112302.
[46] Y. Hangai, Y. Sakaguchi, K. Okada, Y. Tanaka, Press-forming of aluminum foam and estimation of its mechanical properties from X-ray CT images using machine learning, Mater. Charact. (2025) 114781.
[47] G.D. Lai, L.P. Sang, Y.L. Bian, H.L. Xie, J.H. Liu, H.W. Chai, Interfacial debonding and cracking in a solid propellant composite under uniaxial tension: An in situ synchrotron X-ray tomography study, Compos. Sci. Technol. 256 (2024) 110743.
[48] Y. Liu, W. Qian, L. Wang, Y. Xue, C. Hou, S. Wu, In situ X-ray tomography study on internal damage evolution of solid propellant for carrier rockets, Mater. Sci. Eng.: A 882 (2023) 145451.
[49] J. Yeager, S. Luo, B. Jensen, K. Fezzaa, D. Montgomery, D. Hooks, High-speed synchrotron X-ray phase contrast imaging for analysis of low-z composite microstructure, Compos. Part A: Appl. Sci. Manuf. 43 (6) (2012) 885–892.
[50] N.D. Parab, Z.A. Roberts, M.H. Harr, J.O. Mares, A.D. Casey, I.E. Gunduz, M. Hudspeth, B. Claus, T. Sun, K. Fezzaa, et al., High speed X-ray phase contrast imaging of energetic composites under dynamic compression, Appl. Phys. Lett. 109 (13) (2016).
[51] T. Wang, X. Zhang, H. Luo, C. Mao, J. Wang, W. Sheng, K. He, Z. Jiang, In-situ investigation of damage evolution and mechanism in composite propellants under monochromatic X-ray irradiation, Mater. Today Chem. 40 (2024) 102237.
[52] C. Wang, Z. Du, Microscopic interface deterioration mechanism and damage behavior of high-toughness recycled aggregate concrete based on 4D in-situ CT experiments, Cem. Concr. Compos. 153 (2024) 105720.
[53] T. Liu, Y. Li, Z. Chen, J. Zhang, L. Lyu, J. Pei, Damage evolution in asphalt mixtures based on in-situ CT scanning, Constr. Build. Mater. 438 (2024) 137266.
[54] H.-T. Kim, K. Park, Computed tomography (CT) image-based analysis of concrete microstructure using virtual element method, Compos. Struct. 299 (2022) 115937.
[55] Y. Sinchuk, O. Shishkina, M. Gueguen, L. Signor, C. Nadot-Martin, H. Trumel, W. Van Paepegem, X-ray CT based multi-layer unit cell modeling of carbon fiber-reinforced textile composites: Segmentation, meshing and elastic property homogenization, Compos. Struct. 298 (2022) 116003.
[56] S. Samal, Effect of shape and size of filler particle on the aggregation and sedimentation behavior of the polymer composite, Powder Technol. 366 (2020) 43–51.
[57] H. Chai, D. Fan, J. Yuan, L. Hu, H. Xie, G. Du, Q. Feng, W. Zhou, J. Huang, Deformation dynamics of a neutron-irradiated aluminum alloy: An in situ synchrotron tomography study, Acta Mater. 243 (2023) 118493.
[58] D. Gürsoy, F. De Carlo, X. Xiao, C. Jacobsen, Tomopy: a framework for the analysis of synchrotron tomographic data, J. Synchrotron Radiat. 21 (5) (2014) 1188–1193.
[59] A. Buades, B. Coll, J.-M. Morel, A non-local algorithm for image denoising, in: 2005 IEEE Computer Society Conference on Computer Vision and Pattern Recognition, CVPR'05, Vol. 2, Ieee, 2005, pp. 60–65.
[60] E.J. Garboczi, Three-dimensional mathematical analysis of particle shape using X-ray tomography and spherical harmonics: Application to aggregates used in concrete, Cem. Concr. Res. 32 (10) (2002) 1621–1638.
[61] D.N. Theodorou, U.W. Suter, Shape of unperturbed linear polymers: polypropylene, Macromolecules 18 (6) (1985) 1206–1214.
[62] L. Wang, J.Y. Park, Y. Fu, Representation of real particles for DEM simulation using X-ray tomography, Constr. Build. Mater. 21 (2) (2007) 338–346.
[63] H.Y. Li, H.W. Chai, X.H. Xiao, J.Y. Huang, S.N. Luo, Fractal breakage of porous carbonate sand particles: Microstructures and mechanisms, Powder Technol. 363 (2020) 112–121.
[64] H.W. Chai, Z.L. Xie, X.H. Xiao, H.L. Xie, J.Y. Huang, S.N. Luo, Microstructural characterization and constitutive modeling of deformation of closed-cell foams based on in situ x-ray tomography, Int. J. Plast. 131 (2020) 102730.
[65] Y.T. Duan, X.T. Feng, X. Li, B.C. Yang, Mesoscopic damage mechanism and a constitutive model of shale using in-situ X-ray CT device, Eng. Fract. Mech. 269 (2022) 108576.
[66] M. Sambridge, J. Braun, H. McQueen, Geophysical parametrization and interpolation of irregular data using natural neighbours, Geophys. J. Int. 122 (3) (1995) 837–857.
[67] G.R. Johnson, A constitutive model and data for metals subjected to large strains, high strain rates and high temperatures, in: Proceedings of the 7th International Symposium on Ballistics, The Hague, Netherlands, 1983, p. 1983.
[68] G.R. Johnson, W.H. Cook, Fracture characteristics of three metals subjected to various strains, strain rates, temperatures and pressures, Eng. Fract. Mech. 21 (1) (1985) 31–48.
[69] Z. Chen, C. Huang, Z. Shi, H. Liu, J. Niu, B. Li, Z. Tang, Z. Wang, L. Xu, S. Huang, A modified johnson-cook constitutive model of inconel 690 weld overlay taking into account the strain rate softening effect, Mater. Today Commun. 41 (2024) 110551.
[70] L. Tang, C. Ge, H. g. Guo, Q. b. Yu, H. f. Wang, Force chains based mesoscale simulation on the dynamic response of Al-PTFE granular composites, Def. Technol. 17 (1) (2021) 56–63.
[71] E.N. Brown, P.J. Rae, C. Liu, Mixed-mode-I/II fracture of polytetrafluoroethylene, Mater. Sci. Eng.: A 468 (2007) 253–258.
[72] P.J. Rae, D. Dattelbaum, The properties of poly (tetrafluoroethylene)(PTFE) in compression, Polymer 45 (22) (2004) 7615–7625.
[73] P.J. Rae, E.N. Brown, The properties of poly (tetrafluoroethylene)(PTFE) in tension, Polymer 46 (19) (2005) 8128–8140.
[74] X. Yang, Y. He, Y. He, C. Wang, Q. Ling, Z. Guo, Study of the effect of interface properties on the dynamic behavior of Al/PTFE composites using experiment and 3d meso-scale modelling, Compos. Interfaces 27 (4) (2020) 401–418.
[75] Z. Zhang, Y. He, Y. He, L. Guo, C. Ge, H. Wang, Y. Ma, H. Gao, W. Tian, C. Wang, Compressive mechanical properties and shock-induced reaction behavior of Zr/PTFE and Ti/PTFE reactive materials, Materials 15 (19) (2022) 6524.